Phase Transformation Enables Stable Cycling and Fast Charging of Cation Disordered Rocksalt Cathodes

Ji Qian,[$,1] Di Huang,[$,1] Yang Ha,[2] Krishna Prasad Koirala,[3] Inhui Hwang,[4] Chengjun Sun,[4] Chongmin Wang,[5] Wanli Yang,[2] Wei Tong[1,*]

[1] *Energy Technologies and Systems Division, Lawrence Berkeley National Laboratory, Berkeley, CA 94720 USA*
[2] *Advanced Light Source, Lawrence Berkeley National Laboratory, Berkeley, CA 94720 USA*
[3] *Physical and Computational Sciences Directorate, Pacific Northwest National Laboratory, Richland, WA, 99354, USA*
[4] *X-ray Science Division, Advanced Photon Source, Argonne National Laboratory, IL, 60439, USA*
[5] *Environmental Molecular Sciences Laboratory, Pacific Northwest National Laboratory, Richland, WA 99354 USA*
[$] *J. Q. and D. H. contributed equally to this paper*
[*] *Correspondence: weitong@lbl.gov*

ABSTRACT

Developing high-capacity, long-life cathodes is critical to overcome the energy limitations of current Li-ion batteries. Here, we report a Li-excess cation-disordered rocksalt (DRX) cathode, $Li_{1.167}Mn_{0.7}Ti_{0.133}O_{1.8}F_{0.2}$ ($M_{0.7}F_{0.2}$), which demonstrates excellent electrochemical performance. This cathode delivers a capacity approaching 250 mAh g^{-1} and maintains 200 mAh g^{-1} over 200 cycles with an average discharge voltage of 3.1 V at 2 V cutoff. The formation of a spinel-like phase during cycling enables fast charging, achieving over 240 mAh g^{-1} at 2C for 100 cycles. Combined X-ray absorption spectroscopy and transmission electron microscopy reveal reversible electrochemical redox processes and stable Mn local structures during 2 V discharge. These results highlight the potential of DRX cathodes for next-generation Li-ion batteries and provide insights into strategies to overcome kinetic limitations and optimize the cathode-electrolyte interface.

Keywords: Li-ion battery cathode, cation disordered rocksalts, electrochemical kinetics, fast-charging capability, spinel-like phase transformation, cathode-electrolyte interphase

1. INTRODUCTION

Lithium-ion batteries play a crucial role in powering a range of applications, from portable electronics to electric vehicles. However, they still rely on cathode materials such as lithium iron phosphate (LFP) and lithium nickel manganese cobalt oxides (NMC), where were developed over two decades ago.[1-5] Currently, LFP cathode has reached its energy density limit, while conventional layered NMC cathodes dominate energy-intensive applications.[6] However, the reversible capacity of NMC cathodes has been constrained to around 200 mAh g^{-1} to maintain structural stability.[7] To further advance lithium-ion battery technology, new cathode materials are needed to operate at higher capacities without compromising other critical performance metrics.

Extensive search has led to the development of two classes of cathode materials that excel in capacity: Li-rich layered oxides[8-9] and Li-excess cation-disordered rocksalts (DRXs)[10]. Both cathodes consistently deliver high capacities (> 250 mAh g^{-1}) with other performance metrics comparable or not significantly inferior to conventional layered oxides. Li-rich layered oxides share similar atomic arrangements to conventional layered oxides with primary transition metals (TMs) of Mn, Ni, and Co. The presence of Li ions in the TM layers shifts the stoichiometry

toward a Mn-rich regime for charge neutrality. Despite decades of research, Li-rich layered oxides are still hindered by issues like capacity and voltage decay.[11-12] In 2014, Lee *et al.* introduced a new class of high-capacity DRX cathodes.[13] In the rocksalt structure, Li and TM ions occupy a cubic close-packed lattice of octahedral sites, with Li diffusing via an octahedral-tetrahedral-octahedral (o-t-o) hopping mechanism. Sufficient Li excess increases the availability of active 0-TM channels, facilitating macroscopic Li diffusion and enhancing electrochemical performance. Unlike conventional layered oxides, DRX cathodes allow random cation distribution, where 'disorder' specifically refers to cation (Li and TM) mixing, which distinguishes DRX from layered oxides that also adopt a rocksalt structure but retain cation order. Similar to other disordered electrodes,[14] DRX exhibits reduced lattice expansion[15] and less changes in local Li environments across different states of charge.[16] Furthermore, cation disorder in DRX eliminates the need for Co and Ni, which are essential to separate Li sites from the TM sublattice in layered structure. This structural flexibility enables the use of cost-effective and earth-abundant TMs like Mn and Fe[17-21] as redox centers like in lithium manganese oxide and LFP cathodes.[22] Additionally, DRX can accommodate high-valence TMs (e.g.,Ti,[23-24] Nb,[18] V,[25] and Mo,[26-27]) and significant fluorine substitution, expanding its compositional variety.[28-30]

Numerous DRX compositions with varied Li excess and TMs have been reported. Among these, Mn redox-active materials show the most promising performance in terms of capacity, rate capability, and cycling performance.[31-34] Mn is often paired with Nb and Ti metals, and the oxidation states of Mn (Mn^{2+} and Mn^{3+}) in Mn-based DRXs depend on the degree of Li excess and fluorination.[19-20, 35] The extent of fluorination in DRX materials is significantly influenced by the synthetic methods. For example, high energy milling has achieved fluorination levels as high as 34% in Mn^{2+}-based DRX materials,[20, 35] while solid-state synthesis has enabled about 10% fluorination in Mn^{3+}-based DRX materials.[36] Nevertheless, it has been shown that sufficient fluorination can significantly improve the cycling stability of DRX cathodes,[37] while their capacity is less sensitive to the fluorination degree. This is largely attributed to the utilization of more TM redox than oxygen redox and enhanced surface stability by fluorination.[38-41] Oxygen redox tends to dominate when there is a lower amount of redox-active metals or a greater lithium excess.[42] Optimal Li excess typically falls between 10-20%, facilitating sufficient Li ion diffusion and efficient redox utilization.[29] Research on Mn-based DRXs has shown that materials with higher Mn content utilizes more Mn redox and delivers better cycling performance compared to those with lower Mn content.[38] We recently demonstrated stable cycling of a Mn-Ti-based DRX cathode, delivering over 200 mAh g^{-1} for 200 cycles.[43] Building on the promising performance, affordability, and resource availability, efforts are being made to optimize Mn-Ti DRX compositions with even higher Mn content for enhanced capacity and improved cycling stability. Additionally, high-Mn DRX materials exhibit a local structural transformation from rocksalt to spinel-like phase during electrochemical cycling.[44] This phase change has sparked interest in its impact on electrochemical performance, particularly in terms of rate capability, due to the fast Li ion diffusion in spinel structure.[45]

In this work, we report a newly developed DRX compound, $Li_{1.167}Mn_{0.7}Ti_{0.133}O_{1.8}F_{0.2}$ ($M_{0.7}F_{0.2}$), with Li-to-TM ratio of 1.4, which exhibits significantly improved performance. Notably, a capacity above 200 mAh g^{-1} for 200 cycles (90% capacity retention) is achieved at a discharge cutoff voltage of 2 V, enabling a high average discharge voltage of 3.1 V. Additionally, it shows strong potential for fast-charging applications, delivering a capacity over 240 mAh g^{-1} for 100 cycles at a 2C charge rate (730 mA g^{-1}). Using a combination of X-ray absorption spectroscopy (XAS), resonant inelastic X-ray scattering (RIXS), and transmission electron microscopy (TEM)

analyses, we investigate the chemical and structural evolution of this DRX cathode during cycling. These studies address the need to overcome the challenges in kinetic barriers during discharge and surface stability. Our findings reveal the new potential of this class of cathodes and provide valuable insights into possible pathways for further performance improvements.

2. EXPERIMENTAL METHDOS

2.1 Synthesis and Characterization

$Li_{1.167}Mn_{0.7}Ti_{0.133}O_{1.8}F_{0.2}$ cathode material was synthesized by a solid-state reaction using lithium carbonate (Li_2CO_3), manganese oxide (Mn_2O_3), titanium oxide (TiO_2), and lithium fluoride (LiF) as the precursors. Stoichiometric amounts of the precursors except Li_2CO_3 (10% Li excess) are thoroughly mixed and annealed at 1030 °C for 4 h under Ar atmosphere. X-ray diffraction (XRD) patterns were collected on a Bruker D2-Phaser with Cu Kα radiation (λ = 1.54178 Å) from 10 to 80 degree. Conventional Rietveld method was performed to analyze the XRD pattern using the general structure analysis system package with graphical user interface (EXPGUI). Scanning electron microscopy (SEM) image was collected on Zeiss Gemini Ultra-55 Analytical Field Emission Scanning Electron Microscope coupled with the Bruker X-Ray Energy Dispersive Spectrometer with the beam energy of 7 kV.

For TEM analysis, pristine cathode particles were prepared by dispersing them onto lacey carbon copper grids inside an Ar-filled glovebox. The cycled electrodes were disassembled inside a glove box, and then subjected to cross-sectional cutting using a focused ion beam with Xenon plasma as a source. The as-prepared TEM lamella samples were investigated using an aberration corrected Titan 80-300^{TM} scanning/transmission electron microscope operated at 300 kV. HAADF images were collected with a convergence angle of 30 mrad and a collection angle of 68-180 mrad. Electron diffraction images were conducted on a Titan 80-300^{TM} scanning/transmission electron microscope operated at 300 kV using a 10 μm aperture, which produced a probe diameter of ~200 nm. Energy dispersive X-ray spectroscopy (EDS) data were collected using an Oxford X-Max TEM EDS detector. Electron diffraction and fast Fourier transforms (FFT) patterns were processed using the Digital Micrograph software. To prevent beam-induced damage, a probe current of 25 pA was employed throughout the investigation.

2.2 XAS and RIXS Characterization

X-ray absorption near edge structure (XANES) measurements were carried out at 20BM of Advanced Photon Source (APS) at Argonne National Laboratory (ANL). Extended X-ray absorption fine structure (EXAFS) was performed at the Beamline 2-2 and 4-3 in a transmission mode using a (220) monochromator at Stanford Synchrotron Radiation Lightsource (SSRL). *Ex situ* DRX electrodes were removed when the cells reached the designed states of charge, then rinsed by dimethyl carbonate solvent and dried inside an Ar-filled glovebox. Hard XAS data were analyzed using SIXPACK software. RIXS maps were collected on the ultra-high efficiency iRIXS endstation at Beamline 8.0.1 at the Advanced Light Sources (ALS).[46] All samples were sealed in a home-made sample transfer kit inside an Ar-filled glove box, then transferred to the iRIXS vacuum system through the sealed kit to avoid any air exposure. The sample surface was mounted at 45° to the incident beam, and the outgoing photon direction along the RIXS spectrograph was 90°. The resolution of the excitation and emission energy was about 0.2 and 0.35 eV, respectively. An excitation energy step size of 0.2 eV was used for RIXS mapping. All the spectra were normalized to the beam flux measured by the upstream gold mesh, and RIXS

spectra were also normalized to the collection time for each individual cut. Other technical details and parameters could be found in the previous report.[46]

2.3 Electrochemical Characterization

DRX cathode powder was milled with acetylene carbon black (Denka, 50% compressed, surface area: 58 m^2 g^{-1}) to prepare DRX-carbon composite, which was then mixed with polyvinylidene fluoride (PVdF) dissolved in N-methylpyrrolidone solvent to form a slurry with LMNOF: acetylene black: PVdF of 70:20:10 (wt%). The slurry was cast on an aluminum foil using a doctor blade and then dried under vacuum at 120 °C overnight. The dried electrode was assembled using a 2032-type coin cell with Li metal foil, Celgard 2400 separator, and 1 M $LiPF_6$ in 1:2 w/w ethylene carbonate / diethyl carbonate inside an Ar-filled glovebox. The active DRX material loading is ~2.5 mg cm^{-2}. The galvanostatic charge-discharge cycling is performed on an Arbin battery testing station. 1C capacity is defined as 313 mAh g^{-1}. Electrochemical impedance spectra (EIS) measurements were conducted in the pristine and selected discharged states in the frequent range of 1 MHz to 100 mHz with an amplitude voltage of 10 mV using Biologic VMP3.

3. RESULTS AND DISCUSSION

3.1 Synthesis and Structural Characterization

Previous studies indicate that DRX materials synthesized via conventional solid-state method exhibit a fluorine solubility of approximately 10%,[36] and fluorination can suppress gas evolution from the DRX cathode.[35, 38] To optimize the composition of $Li_{2-x-y}Mn_xTi_yO_{2-z}F_z$, a preliminary study on varying Li/Mn/F ratios is performed. To ensure sufficient Li percolation pathway and mitigate oxygen release, we set boundaries of Li ≥ 1.1 and F ≥ 0.1. The goal is to enhance Mn content and thus redox capacity by decreasing Li or TM content while keeping the fluorine at a similar or slightly lower level. As a result, three DRX compositions are designed and synthesized via a solid-state reaction. XRD analysis (**Figure S1A**) confirms pure rocksalt phases for $Li_{1.167}Mn_{0.7}Ti_{0.133}O_{1.8}F_{0.2}$ and $Li_{1.15}Mn_{0.7}Ti_{0.15}O_{1.85}F_{0.15}$. However, a small amount of LiF impurity is observed in $Li_{1.15}Mn_{0.75}Ti_{0.1}O_{1.8}F_{0.2}$ when Mn content is further increased. At a fixed Mn content, higher Li and F levels could enhance capacity and improve capacity retention (**Figure S1B**). Herein, detailed characterization is focused on $Li_{1.167}Mn_{0.7}Ti_{0.133}O_{1.8}F_{0.2}$, denoted as $M_{0.7}F_{0.2}$.

The phase formation of $M_{0.7}F_{0.2}$ material is carefully examined by XRD. As shown in **Figure 1A**, all Bragg peaks are well indexed to the cubic rocksalt phase with the *Fm*3*m* space group, with no secondary phase being detected in the final product. Rietveld refinement shows a good fit to the cubic rocksalt structure (a = 4.1344 Å, R_p = 3.08%). To enhance critical contact within the DRX electrode, the as-prepared DRX material is milled with carbon to form a DRX-carbon composite, resulting in a particle size ranging from a few hundred nanometers to approximately one micrometer (**Figure 1B**). EDS analysis via TEM (**Figure 1C**) shows a uniform elemental distribution across the DRX electrode, with no noticeable segregation. Scanning transmission electron microscopy (STEM) is used to probe the structure at the atomic level. Both the selected area electron diffraction (SAED) pattern (**Figure 1D**) and high-angle annular dark-field (HAADF) image (**Figure 1E**) confirm that the cation arrangement is consistent with the rocksalt phase. Additionally, HAADF image indicates that the milling process does not cause visible damage to the surface of DRX electrode material. The circle-like diffuse scattering effect observed in the SAED pattern and FFT (inset in **Figure 1E**) suggest the presence of cation short-range order (SRO), which is commonly observed in DRX compounds.[47] Overall, XRD and

STEM analyses show that the high-Mn DRX material maintains a long-range cubic rocksalt structure while exhibiting localized SRO.

3.2 Electrochemical Performance

The as-prepared DRX is subjected to electrochemical testing within a voltage range of 4.8 to 1.5 V. Cells are cycled at three different rates, *i.e.*, C/20, C/10, and C/3, based on a theoretical capacity of 321 mAh g^{-1} for 1 Li^+ per formula unit. As shown in **Figure 2A**, the cell capacity increases as the current decreases. The initial discharge capacity reaches 250 and 226 mAh g^{-1} at C/20 and C/10, respectively, but drops to 181 mAh g^{-1} at C/3. During the initial cycles, all cells exhibit an increase in discharge capacity, reaching up to 288, 262, and 212 mAh g^{-1} around 20 cycles. This capacity increase is attributed to enhanced kinetics resulting from a rocksalt to spinel-like phase transformation during early cycling. Such partial spinel-like ordering with short coherence length is beneficial for Li ion diffusion due to the enhanced 0-TM percolation network. More specifically, 16*c*/16*d* disorder (octahedral sites in spinel with F*d*-3*m* space group) creates more accessible environments for Li on tetrahedral and octahedral sites to be in a face-sharing configuration and thus new Li migration channels.[44] The XRD pattern of the DRX electrode at the 30th discharged state (**Figure S2**) shows new Bragg peaks around 18.7° and 35.4°, alongside the characteristic rocksalt peaks. While the presence of only two broad peaks limits the feasibility of a reliable Rietveld refinement, previous studies on similar DRX cathode suggest that these features are indicative of a cation-ordered phase with a spinel-like structure.[40, 44, 48] After this phase transformation stabilizes, the cells show good cycling stability, retaining over 80% of their capacity after 250 cycles.

To further investigate the rate capability, a series of tests are conducted using different charge and discharge protocols. A standard protocol with identical charge/discharge rates (*e.g.*, C/20, C/10, C/5, C/2, 1C, 2C) is employed to determine the capacity at different rates. Two additional protocols with slow charge/varied discharge and varied charge/slow discharge (slow rate is C/20) are designed to isolate the impact of discharge and charge rates, respectively, thus identifying the rate-limiting processes. Rate tests are performed initially and after 20 cycles at C/20 to assess the impact of the rocksalt-to-spinel-like phase transformation. As shown in **Figure 2B**, after the C/20 cycling (following the phase transformation), the cell tested with a slow discharge rate (black in **Figure 2B**) consistently exhibits the highest discharge capacity at all rates, ranging from 265 mAh g^{-1} at C/20 to 219 mAh g^{-1} at 2C, with 82.6% retention at 2C. In contrast, the cell tested at the same charge/discharge rate (blue in **Figure 2B**) delivers the lowest discharge capacity, while the cell cycled with a slow charge rate exhibits intermediate performance. These results indicate that the discharge process is more kinetically limited than the charge process for this high-Mn DRX cathode. Additionally, they underscore the potential of this high-Mn DRX material for fast-charging applications. We then cycle this DRX material at a fast charge rate of 2C (642 mA g^{-1}) (**Figure 2C**). While fast charging slightly delays the phase transformation, the structural mechanism remains unchanged, achieving a maximum capacity of 250 mAh g^{-1} by the 45th cycle, with 240 mAh g^{-1} being maintained after 100 cycles. Notably, the high charge rate does not significantly reduce the discharge capacity.

The DRX electrode is also cycled at different discharge cutoff voltages to examine their impacts on cycling performance. Discharging the DRX electrode to 1.75 and 2 V results in nearly identical performance, with an initial capacity of 215 mAh g^{-1} followed by a slight increase during the first 20 cycles. After 200 cycles, the capacity remains at 200 mAh g^{-1}, corresponding to 93% capacity retention (**Figure 2D**). Remarkably, cycling with a 2 V cutoff leads to a

significant increase in the average discharge voltage, reaching to 3.1 V by the 200th cycle, compared to 2.8 V when discharged to 1.5 V (**Figure S3A**). Interestingly, 2 V discharge cutoff doesn't alter the phase transformation observed with 1.5 V cutoff. As shown in the dQ/dV curves (**Figure S3B&C**), cells cycled with discharge cutoffs of 2 V and 1.5 V display identical features within the voltage range of 2 - 4.8 V. The charge profile starts to evolve during the 2nd charge and stabilizes by the 10th cycle, showing two discrete plateaus at around 4 and 3 V associated with the electrochemical redox of the newly formed spinel-like phase. During discharge, the plateau near 4 V remains stable over extended cycling, while the plateau at ~3 V exhibits gradual capacity decay (**Figure 2F**). This indicates that the reduction process at ~3 V during discharge is crucial for improving long-term cycling performance. When comparing the 1.5 and 2 V discharge cutoff voltages, the most notable difference lies in the discharge profile between 2 and 1.5 V. A close comparison of discharge capacities above 2 V at the 200th cycle reveals that the cell cycled with a 2 V cutoff exhibits a higher discharge capacity than the 1.5 V discharged cell (guided by dash line in **Figure S3D**), although the cell discharged to 1.5 V achieved a higher total capacity due to the additional plateau below 2 V. In contrast, the 1.5 V cell displays a higher charge capacity, primarily in the high-voltage region. These results suggest that the electrochemical processes occurring below 2 V are strongly correlated with those in the high-voltage region and may negatively impact the long-term cycling stability, despite the small capacity gain below 2 V. This electrochemical behavior aligns with a previous study on DRX cathode at various cutoff voltages, suggesting that a reductive process (e.g., ethylene carbonate decomposition) occurs at the DRX surface below 2 V, leading to CO_2 evolution during the subsequent charge.[49] To further investigate the impact of the electrochemical process below 2 V on overall cell performance, we collect the EIS data for DRX cells cycled with discharge cutoffs of 2 V and 1.5 V. As shown in **Figure S4**, both cells exhibit similar impedance in the pristine state. However, upon cycling, the cell discharged to 1.5 V shows a greater impedance buildup than the cell discharged to 2 V, even at the 10th and 20th cycle, which is consistent with the cycling performance.

3.3 Charge Compensation Mechanism

XAS and RIXS are employed to elucidate the charge compensation mechanism for both transition metals and oxygen during cycling. Inverse partial fluorescence yield extracted from RIXS data (iPFY-RIXS) has been established as a bulk probe without the notorious lineshape distortion typically observed in conventional fluorescence yield of XAS, making it particularly useful for quantitative analysis of the bulk Mn state.[50] **Figure 3A** shows the Mn *L*-edge iPFY-RIXS spectra, with reference spectra to determine the formal Mn valance, as previously reported.[51] In the pristine state, the bulk DRX contains Mn primarily in the 3+ oxidation state, as designed. After the 1st charge to 4.8 V, most Mn is oxidized to 4+, with an average oxidation state of 3.83 obtained from spectral fitting. Upon discharge to 2 V, Mn is reduced back to 3+, with a minor fraction of Mn^{2+}, as evidenced by a small shoulder peak at 639.8 eV. The Mn oxidation state after the 1st discharge is estimated to be 3.14. Even after extended cycling, Mn oxidation during charge and reduction during discharge remain dominant. By the 65th discharge, a slight increase in Mn^{2+} is observed compared to the 1st discharge, and the Mn oxidation state after the 65th discharge is 2.97, close to pristine state. Surface-sensitive total electron yield (TEY) of the Mn *L*-edge is also collected to investigate the Mn chemical state at the surface of DRX electrode material (**Figure 3B**). The Mn oxidation state at the surface of pristine DRX is 2+, likely induced by the high energy milling in the presence of carbon black, a reducing agent, during the fabrication of DRX-carbon composite. Interestingly, the Mn^{2+} at the DRX surface is

electrochemically active, undergoing oxidation during charge and reduction during discharge. After extended cycling, accumulation of Mn^{2+} at the surface becomes more evident, particularly after the 65th charge. We also investigate the Mn oxidation state of Mn during cycling with 1.5 V discharge cutoff. In comparison, further Mn reduction to 2+ is more pronounced, especially at the surface, when it's discharged to a lower voltage (**Figure S5A, B**).

Figure 3C shows the O *K*-edge RIXS map at the 1st charged state. The characteristic feature of oxidized O at an emission energy of 524 eV and excitation energy of 531 eV confirms the oxidation of O during the 1st charge.[50] Comparison of the O *K*-edge RIXS cuts in **Figure 3D** reveals the disappearance of this oxidation feature after the 1st discharge, suggesting a reversible O reduction. This O redox process remains electrochemically active after 65 cycles, as shown in **Figure 3E**, where the peak at 524 eV emission energy (red arrows) confirms the O oxidation at 531 eV excitation energy. Unlike some other Li excess TM oxides,[52] the O oxidation and reduction in this DRX electrode are still visible during the 65th cycle, suggesting the good reversibility of O redox process, which contributes to the superior cycling performance. Similarly, electrodes cycled between 4.8 and 1.5 V also exhibit reversible O redox during cycling (**Figure S5C, D**).

XANES and EXAFS data are collected to investigate the chemical states and local environments of Mn/Ti in the bulk electrode upon cycling. In XANES, shifts in absorption edge energy indicate changes in valence state, with a shift to a higher energy suggesting oxidation and lower energy corresponding to reduction. Consistent with the Mn *L*-edge RIXS, the XANES spectra (**Figure 4A**) show a slight decrease in Mn oxidation state after the 65th cycle with 1.5 V cutoff voltage (dash lines) compared to the 2 V discharge (solid lines), which is dominated by Mn^{4+}/Mn^{3+} redox. These results suggest a small reduction of Mn to 2+ occurs when discharged to 1.5 V, possibly contributing to the capacity gain below 2 V. The Ti *K*-edge (**Figure 4B**) remains mostly unchanged, as expected, Ti is electrochemically inactive within the voltage ranges. EXAFS data reveal further insights into the local structure. The Mn *K*-edge EXAFS spectra exhibit two main peaks at 1.4 and 2.7 Å, corresponding to the first shell Mn-O coordination and second shell Mn-TM coordination, respectively. In **Figure 4C, D**, dash and solid lines indicate the EXAFS spectra for discharge cutoffs of 1.5 and 2 V, respectively, with the pristine state shown as a reference (black line). After the 1st charge, the amplitudes of both the Mn-O and Mn-TM peaks increase, indicating more cation order at the charged state, which persists after the 65th charge. After discharge, the local structure of Mn largely reverts back to its pristine state. However, after the 65th discharge, a noticeable difference in the EXAFS is observed. With 1.5 V discharge cutoff, the Mn-O bond length increases and the amplitudes of Mn-O and Mn-TM peaks decrease compared to the pristine state. The increased bond length is consistent with the reduction to Mn^{2+}, which has a larger ionic radius than Mn^{3+}. The lower peak intensities suggest that the 1.5 V cutoff leads to more cation disorder in the Mn local environment after prolonged discharge, whereas the cation rearrangements at 2 V discharge cutoff appear similar to the pristine state. In contrast, the local environment of Ti remains relatively unaffected by electrochemical cycling, except after the 65th discharge at 1.5 V. The amplitude of the Ti-O peak increases after the 65th discharge at 1.5 V, indicating more cation order for Ti. These results suggest that the local environments of Mn and Ti continue to evolve throughout charge and discharge, even after the spinel-like phase formation. Electrochemically induced changes in the TM local coordination are more stable when cycling with 2 V discharge cutoff. In contrast, while discharging to 1.5 V results in more pronounced changes, which may negatively impact electrochemical performance.

3.4 Structural Evolution Upon Cycling

To further investigate the local structural changes after cycling, TEM is employed to examine the atomic arrangements in the DRX electrode after the 65th discharge (**Figure 5**). The SAED patterns for both DRX electrodes cycled with 2 V (**Figure 5A, B**) and 1.5 V (**Figure S6A, B**) discharge cutoff voltage display similar structures. As described in **Figure 1D**, a notable feature is the circle-like diffuse scattering effect, which is characteristic of short-range cation order. In contrast, such diffuse scattering effect disappears, suggesting the absence of short-range cation order in the DRX core, after cycling (**Figure 5A**). Instead, additional diffraction spots (marked by white arrows in **Figure 5B**) are observed on the edge, indicating the formation of spinel-like structure at the surface. This phenomenon has been observed in a similar DRX cathode[40] and is consistent with the XRD result (**Figure S2**) obtained on the cycled DRX electrode as discussed previously. EDS maps of the discharged electrodes reveal that Mn, Ti, O, and F are uniformly distributed with no evidence of elemental segregation or hole formation at either 2 V (**Figure 5C**) or 1.5 V (**Figure S6C**) discharge cutoff, which is essential for achieving good cycling performance. A closer examination of the cycled DRX electrode surface using high-resolution TEM reveals the presence of a cathode-electrolyte interphase (CEI), composed of amorphous/nanocrystalline phases. Notably, the electrode discharged to 1.5 V exhibits a thicker CEI layer (**Figure S6D**) compared to the one discharged to 2 V (**Figure 5D**), indicating the detrimental effect of 1.5 V discharge voltage on the surface structure. Like the EXAFS results, which shows more significant changes in the local structure at 1.5 V discharge cutoff, the TEM observation also supports the electrochemical performance of this cathode at different cutoff voltages. Given previous report of CO_2 evolution triggered by discharging to 1.5 V,[49] it is likely that side reactions below 2 V occur and are accompanied by further Mn reduction.

CONCLUSIONS

We present a new variant of high-Mn DRX cathode, $Li_{1.167}Mn_{0.7}Ti_{0.133}O_{1.8}F_{0.2}$, synthesized by a solid-state reaction. The high Mn content enhances the utilization of the Mn redox mechanism, resulting in excellent electrochemical performance. A capacity of over 200 mAh g^{-1} for 200 cycles has been achieved at 2 V discharge. When the discharge cutoff is lowered to 1.5 V, a higher capacity is achieved, due to the emergence of a pronounced plateau below 2 V. However, the discharge capacity at the 200th cycle with a cutoff of 2 V surpasses that with 1.5 V cutoff, suggesting the electrochemical processes at the plateau below 2 V adversely affects long-term cycling stability. The electrochemical performance aligns with hard and soft XAS results, indicating predominant Mn^{4+}/Mn^{3+} redox activity along with a finite contribution from reversible O redox. A slight reduction to Mn^{2+} is observed after extended cycling, however, this reduction is less pronounced at a cutoff of 2 V compared to 1.5 V. The reversible Mn and O redox, facilitated by high Mn content and fluorination, are crucial to achieving the high electrochemical performance.

Rate capability assessments focusing on the distinct roles of charging and discharging rates reveal its potential for fast-charging applications and the kinetic limitations during discharge. A maximum discharge capacity of 250 mAh g^{-1} has been demonstrated, while 240 mAh g^{-1} is maintained after 100 cycles. The rate tests highlight its potential for fast-charging applications, attributed to the rocksalt-to-spinel-like phase transformation. EXAFS characterization provides insights into the local structural changes around Mn and Ti during cycling and the impact of discharge cutoff voltage. With 2 V discharge cutoff, the cation order around Mn increases during charge and it reverts back during discharge, with minimal local structural change around Ti.

However, discharging to 1.5 V leads to more local structural changes, with Mn more disordered and Ti more ordered after prolonged discharging. High-resolution TEM reveals the formation of a CEI layer composed of amorphous/nanocrystalline phases on the DRX surface. Cycling at 2 V discharge cutoff results in a thinner CEI than 1.5 V cutoff. To further improve the performance, it is necessary to overcome kinetic barriers during discharge and improve structural stability.

ASSOCIATED CONTENT

Supporting Information

XRD pattern, EIS data, Mn *L*-edge iPFY and O *K*-edge RIXS spectra, and HR-TEM images of DRX electrode at varied states of charge. Electrochemical performance under different testing conditions.

Notes

The authors declare no competing financial interest.

ACKNOWLEDGEMENT

This work is supported by the Assistant Secretary for Energy Efficiency and Renewable Energy, Office of Vehicle Technologies of the U.S. Department of Energy under Contract No. DE-AC02-05CH11231. Use of the Stanford Synchrotron Radiation Lightsource, SLAC National Accelerator Laboratory, is supported by the U.S. Department of Energy, Office of Science, Office of Basic Energy Sciences under Contract No. DE-AC02-76SF00515. This research uses resources of the Advanced Light Source, which is a DOE Office of Science User Facility under contract no. DE-AC02-05CH11231. Use of resources at the Molecular Foundry is supported by the Office of Science, Office of Basic Energy Sciences, of the U.S. Department of Energy under Contract No. DE-AC02-05CH11231. STEM work is carried out using the microscopes that are funded in part by a grant from the Washington State Department of Commerce's Clean Energy Fund. Part of the work was conducted at the William R. Wiley Environmental Molecular Sciences Laboratory (EMSL), a national scientific user facility sponsored by DOE's Office of Biological and Environmental Research and located at Pacific Northwest National Laboratory (PNNL). PNNL is operated by Battelle for the U.S. Department of Energy under Contract DE-AC05-76RL01830. This research uses resources of the Advanced Photon Source, an Office of Science User Facility operated for the U.S. Department of Energy (DOE) Office of Science by Argonne National Laboratory, and was supported by the U.S. DOE under Contract No. DE-AC02-06CH11357, and the Canadian Light Source and its funding partners.

REFERENCES

1. Li, M.; Lu, J.; Chen, Z.; Amine, K., 30 Years of Lithium-Ion Batteries. *Adv. Mater.* **2018,** *30*, 1800561.
2. Nayak, P. K.; Erickson, E. M.; Schipper, F.; Penki, T. R.; Munichandraiah, N.; Adelhelm, P.; Sclar, H.; Amalraj, F.; Markovsky, B.; Aurbach, D., Review on Challenges and Recent Advances in the Electrochemical Performance of High Capacity Li- and Mn-Rich Cathode Materials for Li-Ion Batteries. *Adv. Energy Mater.* **2018,** *8*, 1702397.
3. Whittingham, M. S., Lithium Batteries and Cathode Materials. *Chem. Rev.* **2004,** *104* (10), 4271-4302.
4. Xu, J.; Lin, F.; Doeff, M. M.; Tong, W., A Review of Ni-Based Layered Oxides for Rechargeable Li-Ion Batteries. *J. Mater. Chem. A* **2017,** *5*, 874-901.

5. Li, H.; Cormier, M.; Zhang, N.; Inglis, J.; Li, J.; Dahn, J., Is Cobalt Needed in Ni-Rich Positive Electrode Materials for Lithium Ion Batteries? *J. Electrochem. Soc.* **2019,** *166*, A429.
6. Andre, D.; Kim, S.-J.; Lamp, P.; Lux, S. F.; Maglia, F.; Paschos, O.; Stiaszny, B., Future Generations of Cathode Materials: An Automotive Industry Perspective. *J. Mater. Chem. A* **2015,** *3*, 6709-6732.
7. Liu, J.; Bao, Z.; Cui, Y.; Dufek, E. J.; Goodenough, J. B.; Khalifah, P.; Li, Q.; Liaw, B. Y.; Liu, P.; Manthiram, A.; Meng, Y. S.; Subramanian, V. R.; Toney, M. F.; Viswanathan, V. V.; Whittingham, M. S.; Xiao, J.; Xu, W.; Yang, J.; Yang, X.-Q.; Zhang, J.-G., Pathways for Practical High-Energy Long-Cycling Lithium Metal Batteries. *Nat. Energy* **2019,** *4*, 180-186.
8. Croy, J. R.; Balasubramanian, M.; Gallagher, K. G.; Burrell, A. K., Review of the U.S. Department of Energy's "Deep Dive" Effort to Understand Voltage Fade in Li- and Mn-Rich Cathodes. *Acc. Chem. Res.* **2015,** *48*, 2813-2821.
9. van Bommel, A.; Krause, L.; Dahn, J., Investigation of the Irreversible Capacity Loss in the Lithium-Rich Oxide $Li[Li_{1/5}Ni_{1/5}Mn_{3/5}]O_2$. *J. Electrochem. Soc.* **2011,** *158*, A731-A735.
10. Li, H.; Fong, R.; Woo, M.; Ahmed, H.; Seo, D.-H.; Malik, R.; Lee, J., Toward High-Energy Mn-Based Disordered-Rocksalt Li-Ion Cathodes. *Joule* **2022,** *6*, 53-91.
11. Rozier, P.; Tarascon, J. M., Review – Li-Rich Layered Oxide Cathodes for Next-Generation Li-Ion Batteries: Chances and Challenges. *J. Electrochem. Soc.* **2015,** *162*, A2490.
12. Zeng, L.; Liang, H.; Qiu, B.; Shi, Z.; Cheng, S.; Shi, K.; Liu, Q.; Liu, Z., Voltage Decay of Li-Rich Layered Oxides: Mechanism, Modification Strategies, and Perspectives. *Adv. Funct. Mater.* **2023,** *33*, 2213260.
13. Lee, J.; Urban, A.; Li, X.; Su, D.; Hautier, G.; Ceder, G., Unlocking the Potential of Cation-Disordered Oxides for Rechargeable Lithium Batteries. *Science* **2014,** *343*, 519-522.
14. Wang, Z.; Du, Z.; Wang, L.; He, G.; Parkin, I. P.; Zhang, Y.; Yue, Y., Disordered Materials for High-Performance Lithium-Ion Batteries: A Review. *Nano Energy* **2024,** *121*, 109250.
15. Li, N.; Sun, M.; Kan, W. H.; Zhuo, Z.; Hwang, S.; Renfrew, S. E.; Avdeev, M.; Huq, A.; McCloskey, B. D.; Su, D.; Yang, W.; Tong, W., Layered-Rocksalt Intergrown Cathode for High-Capacity Zero-Strain Battery Operation. *Nat. Commun.* **2021,** *12*, 2348.
16. Clément, R.; Lun, Z.; Ceder, G., Cation-Disordered Rocksalt Transition Metal Oxides and Oxyfluorides for High Energy Lithium-Ion Cathodes. *Energy Environ. Sci.* **2020,** *13*, 345-373.
17. Glazier, S. L.; Li, J.; Zhou, J.; Bond, T.; Dahn, J., Characterization of Disordered $Li_{(1+x)}Ti_{2x}Fe_{(1-3x)}O_2$ as Positive Electrode Materials in Li-Ion Batteries Using Percolation Theory. *Chem. Mater.* **2015,** *27*, 7751-7756.
18. Yabuuchi, N.; Takeuchi, M.; Nakayama, M.; Shiiba, H.; Ogawa, M.; Nakayama, K.; Ohta, T.; Endo, D.; Ozaki, T.; Inamasu, T., High-Capacity Electrode Materials for Rechargeable Lithium Batteries: Li_3NbO_4-Based System With Cation-Disordered Rocksalt Structure. *PNAS* **2015,** *112*, 7650-7655.
19. Yabuuchi, N.; Nakayama, M.; Takeuchi, M.; Komaba, S.; Hashimoto, Y.; Mukai, T.; Shiiba, H.; Sato, K.; Kobayashi, Y.; Nakao, A., Origin of Stabilization and Destabilization in Solid-State Redox Reaction of Oxide Ions for Lithium-Ion Batteries. *Nat. Commun.* **2016,** *7*, 13814.

20. Lee, J.; Kitchaev, D. A.; Kwon, D.-H.; Lee, C.-W.; Papp, J. K.; Liu, Y.-S.; Lun, Z.; Clément, R. J.; Shi, T.; McCloskey, B. D.; Guo, J.; Balasubramanian, M.; Ceder, G., Reversible Mn^{2+}/Mn^{4+} Double Redox in Lithium-Excess Cathode Materials. *Nature* **2018,** *556*, 185-190.
21. Lun, Z.; Ouyang, B.; Kwon, D.-H.; Ha, Y.; Foley, E. E.; Huang, T.-Y.; Cai, Z.; Kim, H.; Balasubramanian, M.; Sun, Y.; Huang, J.; Tian, Y.; Kim, H.; McCloskey, B. D.; Yang, W.; Clément, R. J.; Ji, H.; Ceder, G., Cation-Disordered Rocksalt-Type High-Entropy Cathodes for Li-Ion Batteries. *Nat. Mater.* **2021,** *20*, 214-221.
22. Manthiram, A., A Reflection on Lithium-Ion Battery Cathode Chemistry. *Nat. Commun.* **2020,** *11*, 1550.
23. Kobayashi, Y.; Sawamura, M.; Kondo, S.; Harada, M.; Noda, Y.; Nakayama, M.; Kobayakawa, S.; Zhao, W.; Nakao, A.; Yasui, A.; Rajendra, H. B.; Yamanaka, K.; Ohta, T.; Yabuuchi, N., Activation and Stabilization Mechanisms of Anionic Redox for Li Storage Applications: Joint Experimental and Theoretical Study on Li_2TiO_3–$LiMnO_2$ Binary System. *Mater. Today* **2020,** *37*, 43-55.
24. Lee, J.; Seo, D.-H.; Balasubramanian, M.; Twu, N.; Li, X.; Ceder, G., A New Class of High Capacity Cation-Disordered Oxides for Rechargeable Lithium Batteries: Li–Ni–Ti–Mo Oxides. *Energy Environ. Sci.* **2015,** *8*, 3255-3265.
25. Yabuuchi, N.; Takeuchi, M.; Komaba, S.; Ichikawa, S.; Ozaki, T.; Inamasu, T., Synthesis and Electrochemical Properties of $Li_{1.3}Nb_{0.3}V_{0.4}O_2$ as a Positive Electrode Material for Rechargeable Lithium Batteries. *Chem. Commun.* **2016,** *52*, 2051-2054.
26. Hoshino, S.; Glushenkov, A. M.; Ichikawa, S.; Ozaki, T.; Inamasu, T.; Yabuuchi, N., Reversible Three-Electron Redox Reaction of Mo^{3+}/Mo^{6+} for Rechargeable Lithium Batteries. *ACS Energy Lett.* **2017,** *2*, 733-738.
27. Yabuuchi, N.; Tahara, Y.; Komaba, S.; Kitada, S.; Kajiya, Y., Synthesis and Electrochemical Properties of Li_4MoO_5–NiO Binary System as Positive Electrode Materials for Rechargeable Lithium Batteries. *Chem. Mater.* **2016,** *28*, 416-419.
28. Richards, W. D.; Dacek, S. T.; Kitchaev, D. A.; Ceder, G., Fluorination of Lithium‐Excess Transition Metal Oxide Cathode Materials. *Adv. Energy Mater.* **2018,** *8*, 1701533.
29. Ouyang, B.; Artrith, N.; Lun, Z.; Jadidi, Z.; Kitchaev, D. A.; Ji, H.; Urban, A.; Ceder, G., Effect of Fluorination on Lithium Transport and Short-Range Order in Disordered-Rocksalt-Type Lithium-Ion Battery Cathodes. *Adv. Energy Mater.* **2020,** *10*, 1903240.
30. Koirala, K. P.; Jiang, L.; Patil, S.; Longo, P.; Liu, Z.; Freitag, B.; Barthel, J.; Self, E. C.; Du, Y.; Pullan, L.; Tessner, T.; Allen, L. J.; Xu, W.; Tong, W.; Nanda, J.; Wang, C., Direct Mapping of Fluorine in Cation Disordered Rocksalt Cathodes. *ACS Energy Lett.* **2024,** *9*, 10-16.
31. Crafton, M. J.; Yue, Y.; Huang, T.-Y.; Tong, W.; McCloskey, B. D., Anion Reactivity in Cation-Disordered Rocksalt Cathode Materials: The Influence of Fluorine Substitution. *Adv. Energy Mater.* **2020,** *10*, 2001500.
32. Yue, Y.; Li, N.; Li, L.; Foley, E. E.; Fu, Y.; Battaglia, V. S.; Clément, R. J.; Wang, C.; Tong, W., Redox Behaviors in Li-Excess Cation-Disordered Mn-Nb-OF Rocksalt Cathode. *Chem. Mater.* **2020,** *32*, 4490-4498.
33. Huang, T.-Y.; Crafton, M. J.; Yue, Y.; Tong, W.; McCloskey, B. D., Deconvolution of Intermixed Redox Processes in Ni-Based Cation-Disordered Li-Excess Cathodes. *Energy Environ. Sci.* **2021,** *14*, 1553-1562.

34. Yue, Y.; Ha, Y.; Huang, T.-Y.; Li, N.; Li, L.; Li, Q.; Feng, J.; Wang, C.; McCloskey, B. D.; Yang, W.; Tong, W., Interplay Between Cation and Anion Redox in Ni-Based Disordered Rocksalt Cathodes. *ACS Nano* **2021,** *15*, 13360-13369.
35. Yue, Y.; Li, N.; Ha, Y.; Crafton, M. J.; McCloskey, B. D.; Yang, W.; Tong, W., Tailoring the Redox Reactions for High-Capacity Cycling of Cation-Disordered Rocksalt Cathodes. *Adv. Funct. Mater.* **2021,** *31*, 2008696.
36. Szymanski, N. J.; Zeng, Y.; Bennett, T.; Patil, S.; Keum, J. K.; Self, E. C.; Bai, J.; Cai, Z.; Giovine, R.; Ouyang, B.; Wang, F.; Bartel, C. J.; Clément, R. J.; Tong, W.; Nanda, J.; Ceder, G., Understanding the Fluorination of Disordered Rocksalt Cathodes through Rational Exploration of Synthesis Pathways. *Chem. Mater.* **2022,** *34*, 7015-7028.
37. Lee, J.; Papp, J. K.; Clément, R. J.; Sallis, S.; Kwon, D.-H.; Shi, T.; Yang, W.; McCloskey, B. D.; Ceder, G., Mitigating Oxygen Loss to Improve the Cycling Performance of Hhigh Capacity Cation-Disordered Cathode Materials. *Nat. Commun.* **2017,** *8*, 981.
38. Lun, Z.; Ouyang, B.; Kitchaev, D. A.; Clément, R. J.; Papp, J. K.; Balasubramanian, M.; Tian, Y.; Lei, T.; Shi, T.; McCloskey, B. D.; Lee, J.; Ceder, G., Improved Cycling Performance of Li-Excess Cation-Disordered Cathode Materials upon Fluorine Substitution. *Adv. Energy Mater.* **2019,** *9*, 1802959.
39. Crafton, M. J.; Huang, T.-Y.; Yue, Y.; Giovine, R.; Wu, V. C.; Dun, C.; Urban, J. J.; Clément, R. J.; Tong, W.; McCloskey, B. D., Tuning Bulk Redox and Altering Interfacial Reactivity in Highly Fluorinated Cation-Disordered Rocksalt Cathodes. *ACS Appl. Mater. Interfaces* **2023,** *15*, 18747-18762.
40. Li, L.; Lun, Z.; Chen, D.; Yue, Y.; Tong, W.; Chen, G.; Ceder, G.; Wang, C., Fluorination-Enhanced Surface Stability of Cation-Disordered Rocksalt Cathodes for Li-Ion Batteries. *Adv.d Funct. Mater.* **2021,** *31*, 2101888.
41. Li, L.; Ahn, J.; Yue, Y.; Tong, W.; Chen, G.; Wang, C., Fluorination-Enhanced Surface Stability of Disordered Rocksalt Cathodes. *Adv. Mater.* **2022,** *34*, 2106256.
42. Xu, J.; Sun, M.; Qiao, R.; Renfrew, S. E.; Ma, L.; Wu, T.; Hwang, S.; Nordlund, D.; Su, D.; Amine, K.; Lu, J.; McCloskey, B. D.; Yang, W.; Tong, W., Elucidating Anionic Oxygen Activity in Lithium-Rich Layered Oxides. *Nat. Commun.* **2018,** *9*, 947.
43. Qian, J.; Ha, Y.; Koirala, K. P.; Huang, D.; Huang, Z.; Battaglia, V. S.; Wang, C.; Yang, W.; Tong, W., Toward Stable Cycling of a Cost-Effective Cation-Disordered Rocksalt Cathode via Fluorination. *Adv. Funct. Mater.* **2023,** *33*, 2205972.
44. Cai, Z.; Ouyang, B.; Hau, H.-M.; Chen, T.; Giovine, R.; Koirala, K. P.; Li, L.; Ji, H.; Ha, Y.; Sun, Y.; Huang, J.; Chen, Y.; Wu, V.; Yang, W.; Wang, C.; Clément, R. J.; Lun, Z.; Ceder, G., In Situ Formed Partially Disordered Phases as Earth-Abundant Mn-Rich Cathode Materials. *Nat. Energy* **2024,** *9*, 27-36.
45. Thackeray, M. M., Spinel Electrodes for Lithium Batteries. *J. Am. Ceram. Soc.* **1999,** *82*, 3347-3354.
46. Qiao, R.; Li, Q.; Zhuo, Z.; Sallis, S.; Fuchs, O.; Blum, M.; Weinhardt, L.; Heske, C.; Pepper, J.; Jones, M.; Brown, A.; Spucces, A.; Chow, K.; Smith, B.; Glans, P.-A.; Chen, Y.; Yan, S.; Pan, F.; Piper, L. F. J.; Denlinger, J.; Guo, J.; Hussain, Z.; Chuang, Y.-D.; Yang, W., 1. Qiao, R.; Li, Q.; Zhuo, Z.; Sallis, S.; Fuchs, O.; Blum, M.; Weinhardt, L.; Heske, C.; Pepper, J.; Jones, M.; Brown, A.; Spucces, A.; Chow, K.; Smith, B.; Glans, P.-A.; Chen, Y.; Yan, S.; Pan, F.; Piper, L. F. J.; Denlinger, J.; Guo, J.; Hussain, Z.; Chuang, Y.-D.; Yang, W., High-Efficiency in situ Resonant Inelastic X-Ray Scattering (iRIXS) Endstation at the Advanced Light Source. *Rev. Sci. Instrum.* **2017,** *88*, 033106.

47. Ji, H.; Urban, A.; Kitchaev, D. A.; Kwon, D.-H.; Artrith, N.; Ophus, C.; Huang, W.; Cai, Z.; Shi, T.; Kim, J. C.; Kim, H.; Ceder, G., Hidden Structural and Chemical Order Controls Lithium Transport in Cation-Disordered Oxides for Rechargeable Batteries. *Nat. Commun.* **2019,** *10*, 592.
48. Li, T.; Geraci, T. S.; Koirala, K. P.; Zohar, A.; Bassey, E. N.; Chater, P. A.; Wang, C.; Navrotsky, A.; Clément, R. J., Structural Evolution in Disordered Rock Salt Cathodes. *J. Am. Chem. Soc.* **2024,** *146*, 24296-24309.
49. Crafton, M. J.; Huang, T.-Y.; Cai, Z.; Konz, Z. M.; Guo, N.; Tong, W.; Ceder, G.; McCloskey, B. D., Dialing in the Voltage Window: Reconciling Interfacial Degradation and Performance Decay for Cation-Disordered Rocksalt Cathodes. *J. Electrochem. Soc.* **2024,** *171*, 020530.
50. Yang, W.; Devereaux, T. P., Anionic and Cationic Redox and Interfaces in Batteries: Advances From Soft X-Ray Absorption Spectroscopy to Resonant Iinelastic Scattering. *J. Power Sources* **2018,** *389*, 188-197.
51. Li, Q.; Qiao, R.; Wray, L. A.; Chen, J.; Zhuo, Z.; Chen, Y.; Yan, S.; Pan, F.; Hussain, Z.; Yang, W., Quantitative Probe of the Transition Metal Redox in Battery Electrodes Through Soft X-Ray Absorption Spectroscopy. *J. Phys. D: Appl. Phys.* **2016,** *49*, 413003.
52. Yan, P.; Zheng, J.; Tang, Z.-K.; Devaraj, A.; Chen, G.; Amine, K.; Zhang, J.-G.; Liu, L.-M.; Wang, C., Injection of Oxygen Vacancies in the Bulk Lattice of Layered Cathodes. *Nat. Nanotechnol.* **2019,** *14*, 602-608.

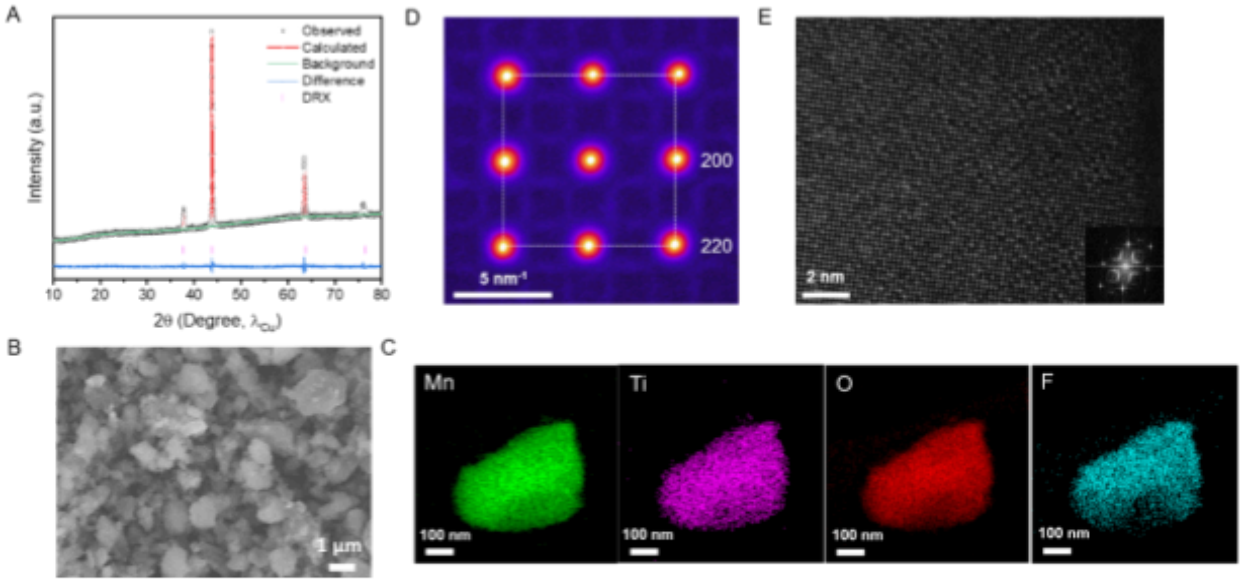

Figure 1. Synthesis and physical characterization of $Li_{1.167}Mn_{0.7}Ti_{0.133}O_{1.8}F_{0.2}$. (A) XRD pattern and Rietveld refinement analysis based on *Fmm* (a = 4.1344 Å, R_p = 3.08%). (B) SEM image after milled with carbon. (C) EDS maps of Mn (green), Ti (magenta), O (red), and F (cyan). (D) SAED pattern, showing disordered rocksalt structure with short-range order. (E) Representative HAADF-STEM image and inset FFT pattern.

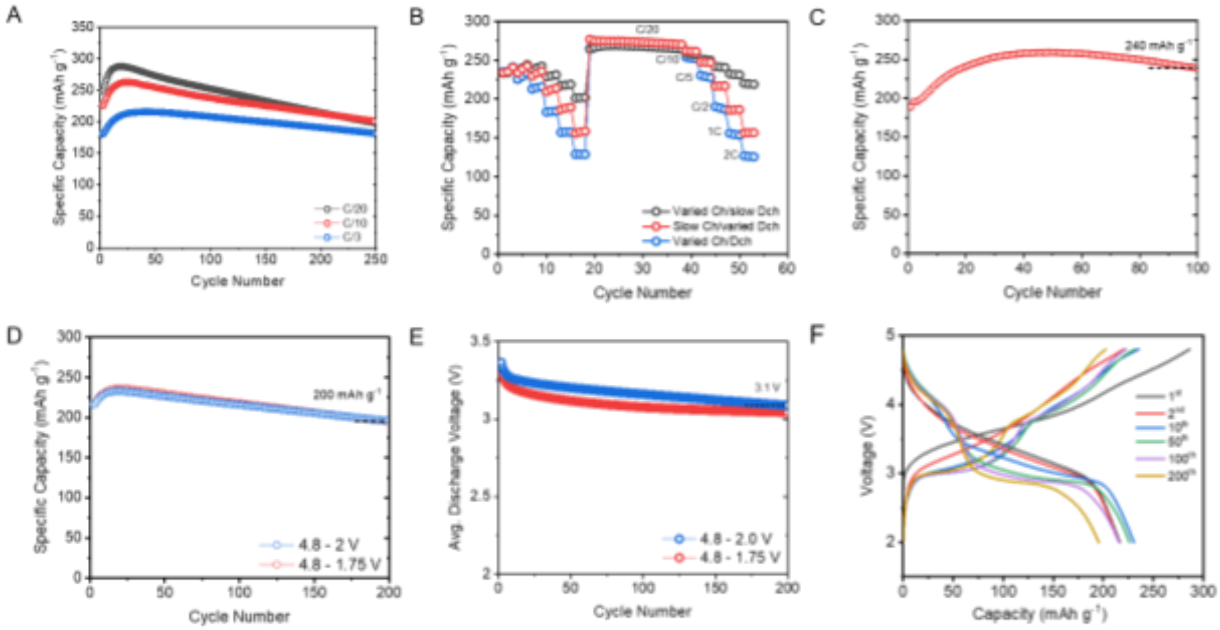

Figure 2. Electrochemical performance of $Li_{1.167}Mn_{0.7}Ti_{0.133}O_{1.8}F_{0.2}$. (A) Specific discharge capacity at different rates. (B) Specific discharge capacity at varied rates ranging from C/20 to 2C, slow charge/discharge is C/20. (C) Specific discharge capacity at 2C charge. (D) Specific discharge capacity at varied discharge cutoff voltages. (E) Average discharge voltage at varied discharge cutoff voltages. (F) Charge-discharge voltage profiles between 4.8 and 2 V at selected cycles. The cells are cycled within 4.8 and 1.5 V at C/20, unless noted otherwise.

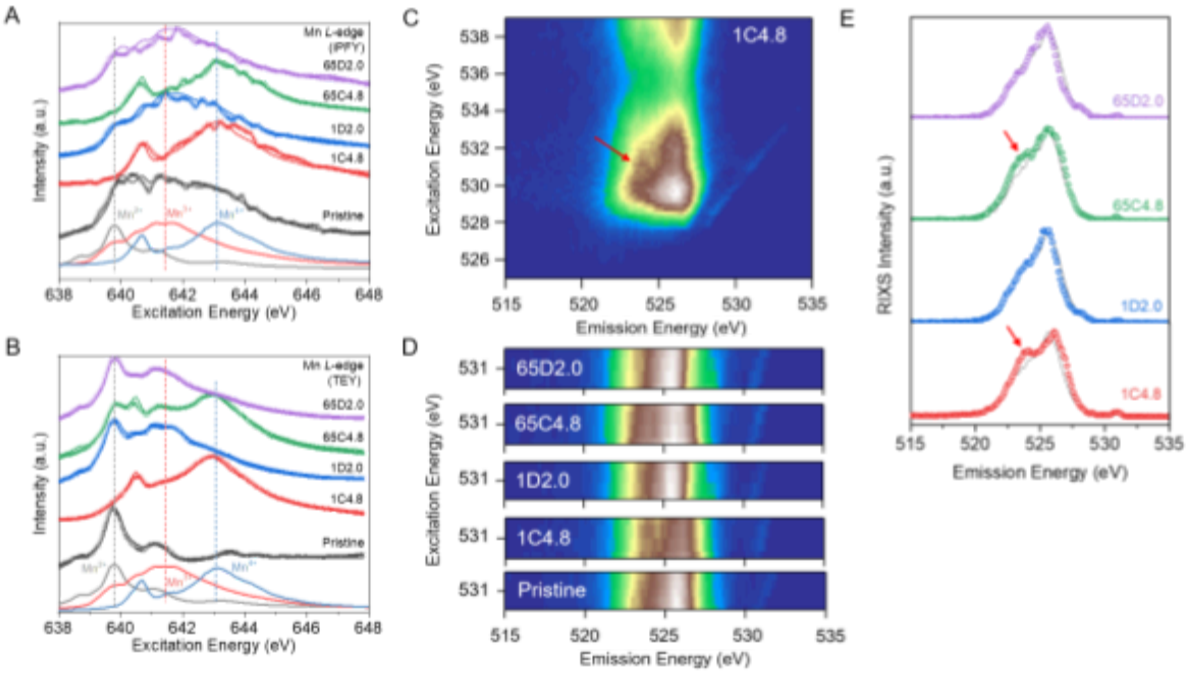

Figure 3. Chemical states of Mn and O at selected states of charge. (A) Mn *L*-edge iPFY spectra. (B) Mn *L*-edge TEY spectra. (C) Full O *K*-edge RIXS map at the first charge, red arrow indicates the O redox feature. (D) Partial O *K*-edge RIXS maps. (E) Corresponding O *K*-edge RIXS cut at 531.0 eV excitation energy. The dots and fine lines in (A, B) label the experimental and fitted spectra, respectively, while the dots in (E) label the experimental data and fine lines label the experimental data in the pristine state for reference to guide the comparison. The cells are cycled at C/20 between 4.8 V and 2 V. Samples are labelled by the number of charge (C) or discharge (D) followed by the voltage, e.g., 1C4.8 indicates the 1st charge at 4.8 V.

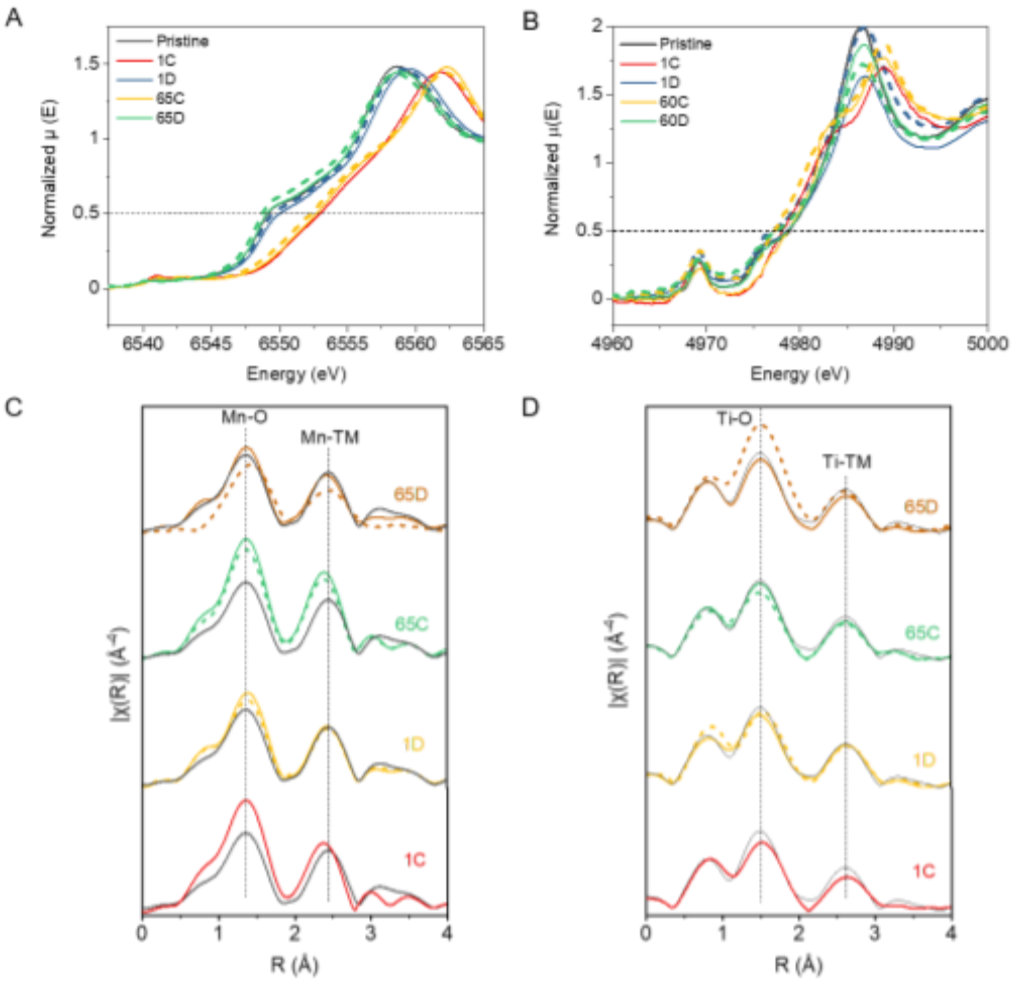

Figure 4. Local structural environment evolution for Mn and Ti upon cycling. (A) XANES spectra of Mn. (B) XANES spectra of Ti. (C) EXAFS spectra of Mn. (D) EXAFS spectra of Ti. Solid and dashed lines indicate 2 V and 1.5 V cutoff, respectively. Black lines in (C, D) label the spectra in pristine state for reference to guide the comparison. Horizontal short dashed lines in (A, B) guide the changes in energy shift at half maximum height, while the vertical ones in (C, D) guide the changes in Mn-O and Mn-TM bond length.

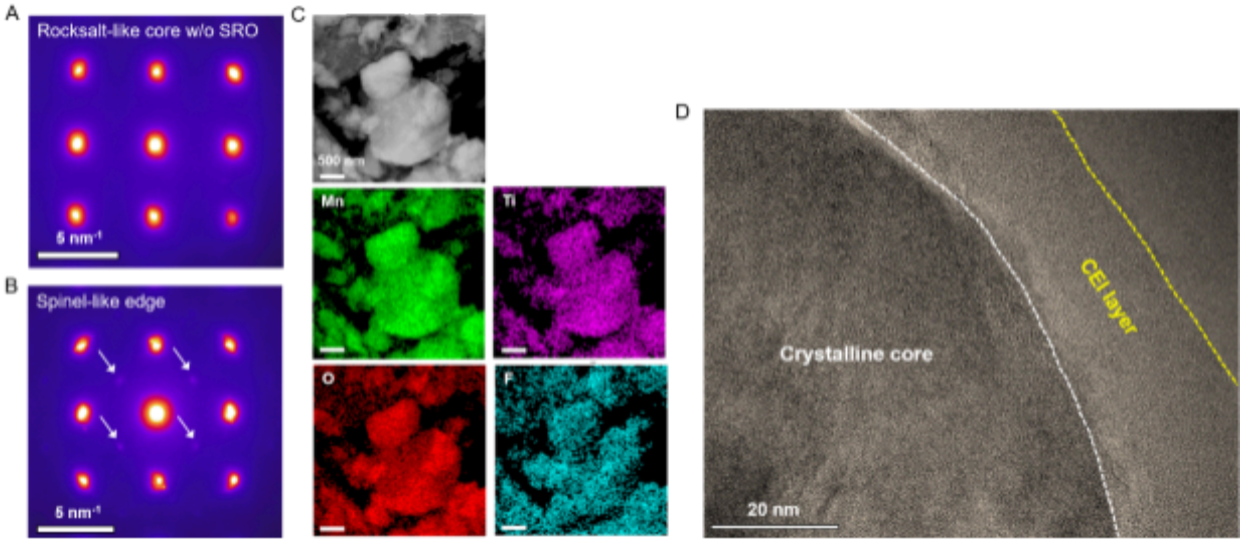

Figure 5. Structural evolution upon cycling. (A) SEAD patterns, showing a rocksalt-like core without short-range order. (B) SEAD patterns, showing a spinel-like edge marked by white arrows. (C) TEM image and EDS maps of Mn (green), Ti (magenta), O (red), and F (cyan). (D) HR-TEM image, showing the crystalline core with an amorphous/nanocrystalline CEI layer on the surface. The cell is cycled at C/20 within 4.8 and 2 V for 65 cycles.

For Table of Contents Only

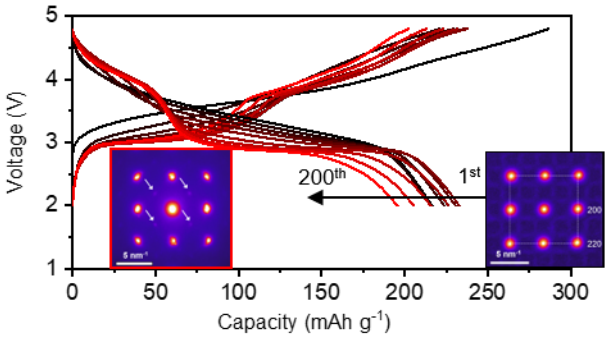

Supporting Information for

Phase Transformation Enables Stable Cycling and Fast Charging of Cation Disordered Rocksalt Cathodes

Ji Qian,[$,1] Di Huang,[$,1] Yang Ha,[2] Krishna Prasad Koirala,[3] Inhui Hwang,[4] Chengjun Sun,[4] Chongmin Wang,[5] Wanli Yang,[2] Wei Tong[1,*]

[1] *Energy Technologies and Systems Division, Lawrence Berkeley National Laboratory, Berkeley, CA 94720 USA*
[2] *Advanced Light Source, Lawrence Berkeley National Laboratory, Berkeley, CA 94720 USA*
[3] *Physical and Computational Sciences Directorate, Pacific Northwest National Laboratory, Richland, WA, 99354, USA*
[4] *X-ray Science Division, Advanced Photon Source, Argonne National Laboratory, IL, 60439, USA*
[5] *Environmental Molecular Sciences Laboratory, Pacific Northwest National Laboratory, Richland, WA 99354 USA*
[$] *J. Q. and D. H. contributed equally to this paper*
[*] *Correspondence: weitong@lbl.gov*

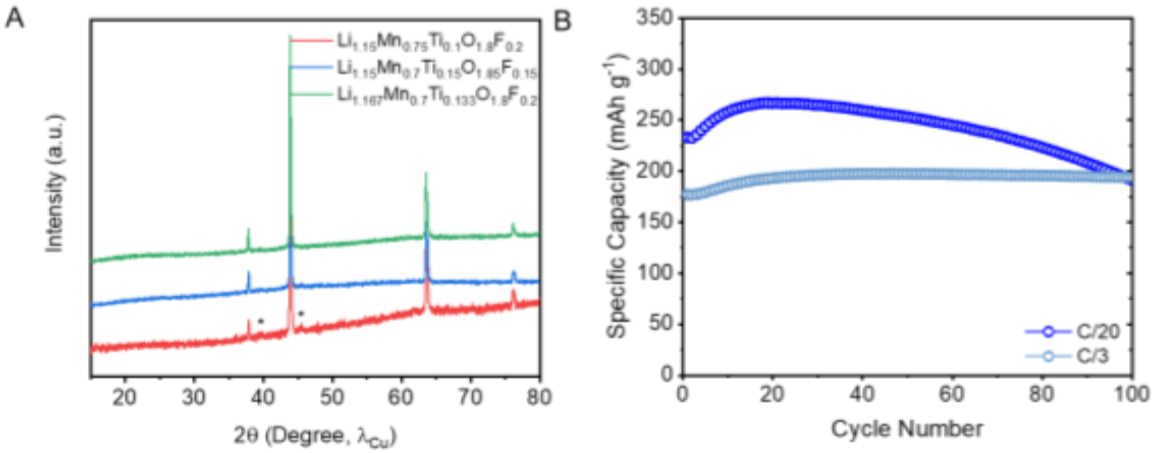

Figure S1. Phase formation of $Li_{2-x-y}Mn_xTi_yO_{2-z}F_z$ (Li ≥ 1.1, F ≥ 0.1). (A) XRD patterns, confirming formation of a pure cubic rocksalt phase in all studied compositions, except for $Li_{1.15}Mn_{0.75}Ti_{0.1}O_{1.8}F_{0.2}$, where a secondary LiF phase is observed (marked by asterisks). (B) Electrochemical performance of $Li_{1.15}Mn_{0.7}Ti_{0.15}O_{1.85}F_{0.15}$ cathode, cells are cycled within 4.8 and 1.5 V at varied rates.

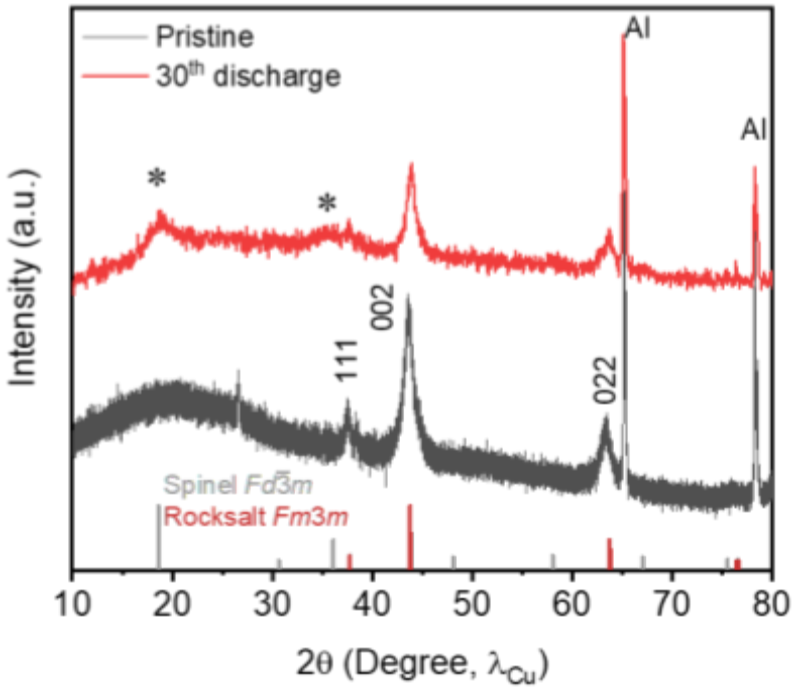

Figure S2. Structural evolution of $Li_{1.167}Mn_{0.7}Ti_{0.133}O_{1.8}F_{0.2}$ electrode during cycling. XRD patterns in the pristine and 30th discharge states, where Bragg peaks corresponding to the rocksalt are labeled with hkl indices, asterisks (∗) indicate the peaks associated with the newly formed spinel-like phase, vertical lines on the bottom show the characteristic peaks of spinel and rocksalt phases.

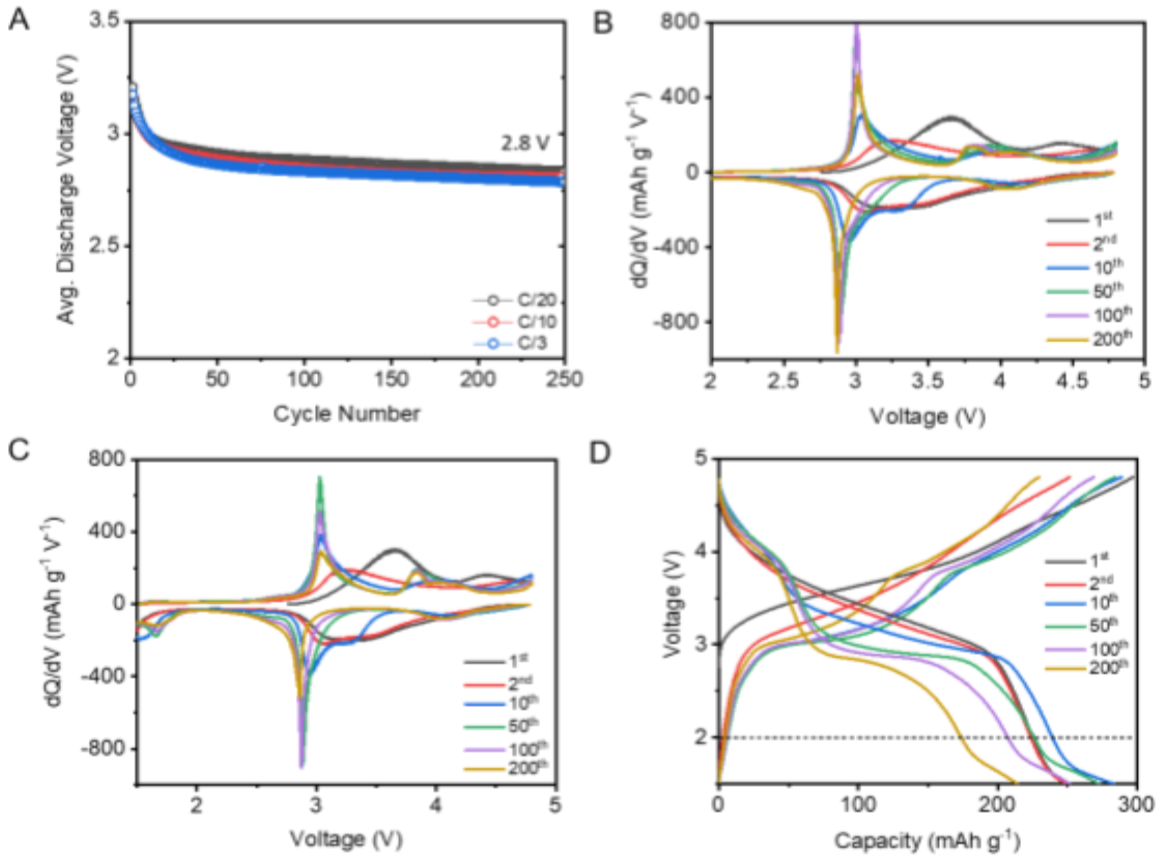

Figure S3. Electrochemical performance of $Li_{1.167}Mn_{0.7}Ti_{0.133}O_{1.8}F_{0.2}$. (A) Average discharge voltage at different rates. (B) Differential capacity curves measured between 4.8 V and 2 V. (C) Differential capacity curves measured between 4.8 V and 1.5 V. (D) Charge-discharge voltage profiles, the discharge capacity above 2 V is guided by dash line. The cells are cycled within 4.8 and 1.5 V at C/20, unless noted otherwise.

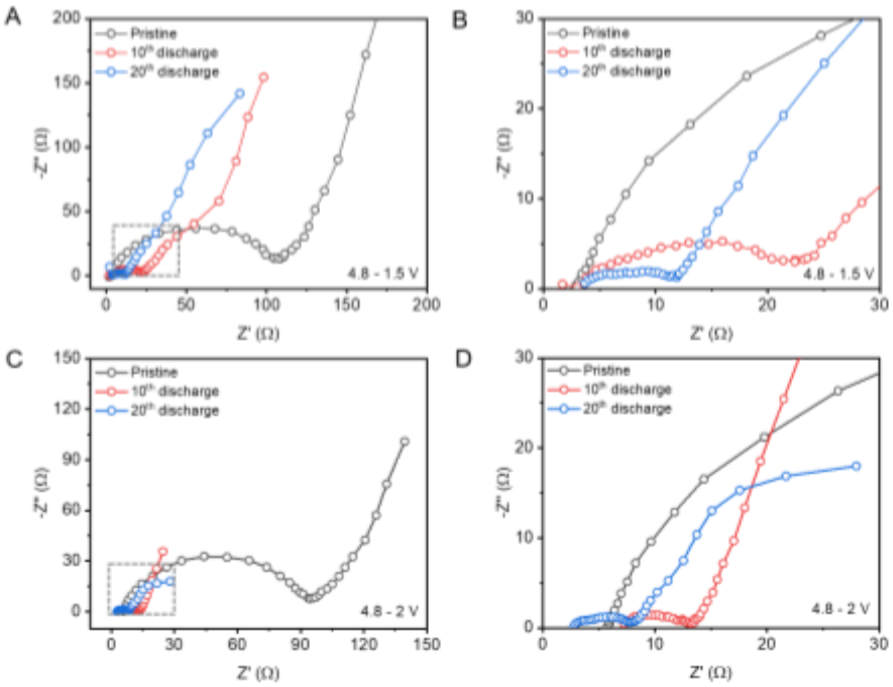

Figure S4. Impact of discharge cutoff voltage on cell impedance during cycling. (A, B) EIS spectra measured between 4.8 V and 1.5 V at the selected states of charge. (C, D) EIS spectra measured between 4.8 V and 2 V at the selected states of charge.

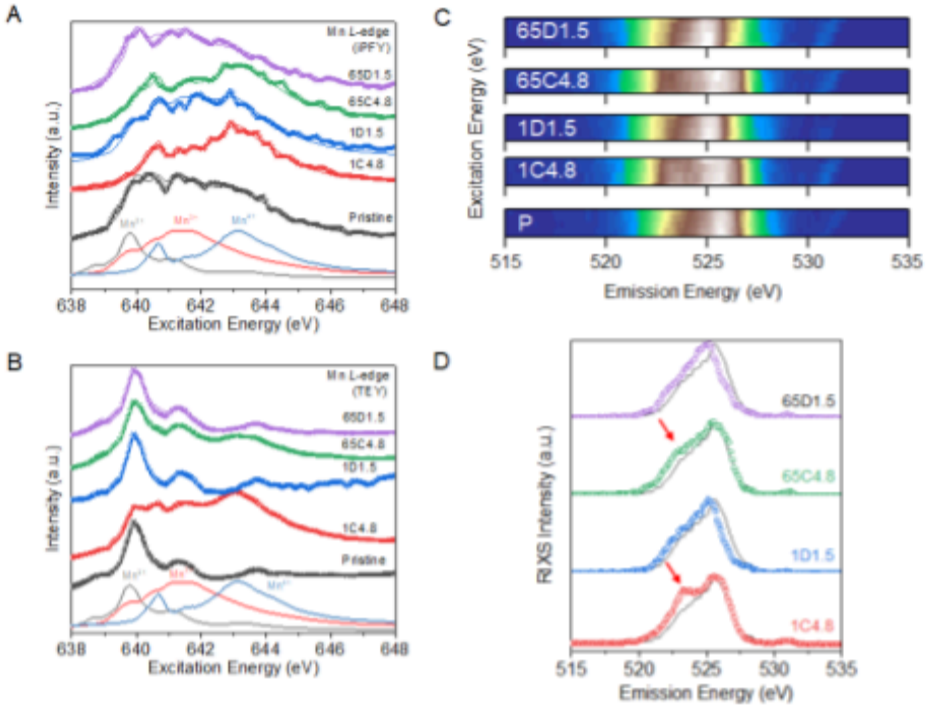

Figure S5. Chemical states of Mn and O at selected states of charge. (A) Mn *L*-edge iPFY spectra. (B) Mn *L*-edge TEY spectra. (C) Partial O *K*-edge RIXS maps. (D) Corresponding O *K*-edge RIXS cut at 531.0 eV excitation energy, red arrow indicates the O redox feature. The dots and fine lines in (A, B) label the experimental and fitted spectra, respectively, while the dots in (D) label the experimental data and fine lines label the experimental data in the pristine state for reference to guide the comparison. The cells are cycled at C/20 between 4.8 V and 1.5 V. Samples are labelled by the number of charge (C) or discharge (D) followed by the voltage, e.g., 1C4.8 indicates the 1st charge at 4.8 V.

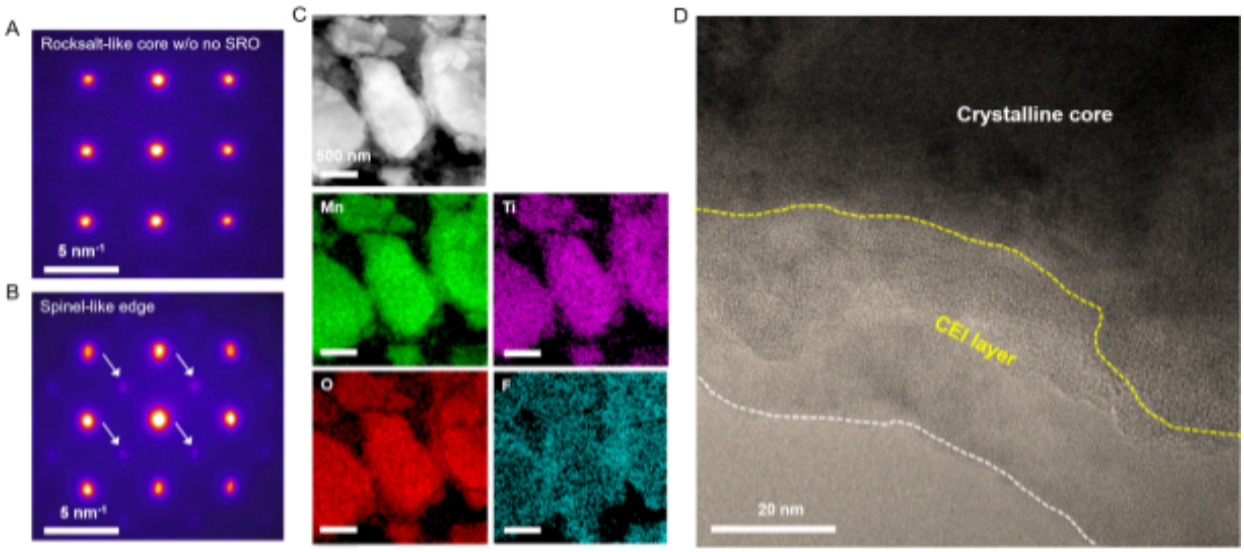

Figure S6. Structural evolution upon cycling. (A) SEAD patterns, showing a rocksalt-like core without short-range order. (B) SEAD patterns, showing a spinel-like edge marked by white arrows. (C) TEM image and EDS maps of Mn (green), Ti (magenta), O (red), and F (cyan). (D) HR-TEM image, showing the crystalline core with a thick amorphous/nanocrystalline CEI layer on the surface. The cell is cycled at C/20 within 4.8 and 1.5 V for 65 cycles.